Spurious Signals in TRMM/VIRS Reflectance Channels and Their Effect on Aerosol Retrievals

ALEXANDER IGNATOV

NOAA/NESDIS/Office of Research and Applications, Camp Springs, Maryland

ABSTRACT

Aerosol optical depths, τ_1 and τ_2, and the Ångström exponent $\alpha = -\ln(\tau_1/\tau_2)/\ln(\lambda_1/\lambda_2)$, are retrieved from daytime measurements (sun zenith angle $\theta_o < 60°$) over ocean in reflectance bands 1 ($\lambda_1 = 0.63$ μm) and 2 ($\lambda_2 = 1.61$ μm) of the five-channel visible and infrared scanner (VIRS) on board the Tropical Rainfall Measuring Mission (TRMM) satellite. In band 2, a thermal leak originating from the secondary spectral response peak at ~5.2 μm contributes radiance comparable to the signal scattered by aerosols. In the past two corrections, the thermal signal was parameterized empirically as a linear function of radiances in bands 4 and 5 (centered at 10.8 and 11.9 μm, respectively), R_4 and R_5, and a quadratic function of view angle θ through multiple regression analyses. The regression coefficients were estimated from a limited amount of *all-sky* nighttime ($100° < \theta_o < 170°$) data over land and ocean, and were used to predict and remove the false signal from daytime data. As a result, retrievals of τ_2 and α have been improved, but they still remain seriously flawed.

This study reexamines the nighttime signal in VIRS channel 2 using two representative 9-day segments of the TRMM single scanner footprint (SSF) data collected from 4–12 February and 2–10 April 1998. The past parameterizations did not always perform accurately. Their residuals are biased and skewed, and reveal artificial trends with time, latitude, θ, R_4, and R_5. A new parameterization of the nighttime signal is proposed that makes use of 1) *clear-sky* ocean data only (rather than previously used all sky, full set); 2) more accurate principal component analyses (PCA) to approximate the θ, R_4, and R_5 dependencies of the false signal (in place of the formerly used liner/quadratic regressions); and 3) explicit accounting for temporal instability of the spurious signal (rather than assuming it to be stable as was done in the past). The new parameterization substantially relieves the problems found in the previous two parameterizations. A much smaller false signal of unknown origin, found in channel 1, is also analyzed and parameterized in this study, consistently with channel 2. The effects of false signals and residuals of different corrections on retrieved τ and α are preliminarily estimated using an approximate formulation based on a simplified treatment of the radiative transfer equation.

1. Introduction

The Tropical Rainfall Measuring Mission (TRMM) satellite was launched in November 1997 (Kummerow et al. 2000). One of the mission's objectives is measuring the radiant energy exchange in tropical and subtropical regions of the world with the Clouds and the Earth's Radiant Energy System (CERES) instrument (Wielicki et al. 1996). The five-channel visible and infrared scanner (VIRS), similar to the Advanced Very High Resolution radiometer (AVHRR) on the National Oceanic Atmospheric Administration (NOAA) satellites, is also on board TRMM (Kummerow et al. 1998; Barnes et al. 2000).

For an average TRMM orbit altitude of ~350 km, the nominal resolution for CERES and VIRS is ~10 and ~2 km at nadir, and it degrades as the view angle increases (e.g., Minnis et al. 2002). The National Aeron-

auties and Space Administration (NASA) Langley Research Center (LaRC) produces a TRMM single scanner footprint (SSF) dataset by mapping statistics of finer-resolution VIRS data into coarser-resolution CERES footprints, and organizing the merged CERES–VIRS data into 1-h granules (files) (Geier et al. 2001). Each SSF is time and georeferenced, and also contains, along with CERES radiances and sun-view geometries, average VIRS radiances in channels 1–5, and their variances. Two VIRS statistics are reported: one is for the full VIRS sample over a CERES footprint (*all sky*), and the other is for its cloud-free subsample only (*clear sky*). Over ocean during daytime, the clear-sky radiances in VIRS reflectance channels centered at $\lambda_1 = 0.63$ and $\lambda_2 = 1.61$ μm are used for aerosol retrievals (Ignatov and Stowe 2000). Combining CERES radiative fluxes with VIRS aerosols on the SSF is useful for a number of applications such as estimating the top-of-the-atmosphere aerosol radiative forcing, molecular albedo, angular distribution models, and surface fluxes (e.g., Loeb and Kato 2002; Kato et al. 2002; Rutan and Char-

Corresponding author address: Dr. Alex Ignatov, NOAA, E/RA1, WWBG, Rm. 712R, 5200 Auth Rd., Camp Springs, MD 20746-4304. E-mail: Alex.Ignatov@noaa.gov

lock 2002). Accuracy of the retrieved aerosol optical depths (AODs) in channels 1 and 2, τ_1 and τ_2, and the Ångström exponent, $\alpha = -\ln(\tau_1/\tau_2)/\ln(\lambda_1/\lambda_2)$, is the key to the validity of such quantitative studies.

VIRS channel 2 is strongly contaminated by the thermal leak originating from the secondary spectral response peak at ~ 5.2 μm (Barnes et al. 2000, see their Figs. 4 and 5). Under cloud-free oceanic conditions used for aerosol retrievals, the relative contamination is maximal because the thermal signal from the warm surface is at its largest whereas the reflected signal from the dark ocean is at its lowest. The false signal (interpreted as due to aerosol) causes error in the retrieved τ_2 of more than 100% (Ignatov and Stowe 2000, and section 3 below). It must be corrected before any aerosol analyses are possible in VIRS channel 2.

Based on the analyses of a restricted set of nighttime scans over the Indian Ocean on 2 February 1998, Barnes et al. (2000) concluded that either "an extended set of nighttime measurements or an external source of columnar water vapor values will be required to provide an adequate correction for the band 2 thermal leak." The vertical profiles of temperature and water vapor (along with aerosols, minor gases, and residual cloud) are not easy to accurately specify in each CERES footprint, even for a cloud-free atmosphere, and the radiative transfer model may be not sufficiently accurate. An empirical approach based on the statistical correlative analyses thus appears most consistent with the practical objective of correction. Such an approach is currently being used, for instance, with the Moderate Resolution Imaging Spectroradiometer (MODIS) flown on board the *Terra* and *Aqua* satellites (J. Xiong and W. Barnes 2002, personal communication) whose bands 5, 6, 7, and 26 (centered at 1.24, 1.64, 2.13, and 1.38 μm, respectively) are contaminated by the thermal leak centered at 5.3 μm. The false signals are predicted and empirically removed from daytime data using measurements in MODIS band 28 centered at ~ 7.2 μm, which is sensitive to approximately the same atmospheric layer as the 5.3-μm leak: ~ 400 mb ($H \sim 7$ km) for a wet atmosphere, and ~ 750 mb ($H \sim 2.5$ km, with some contribution from the surface) for a dry atmosphere (C. Moeller 2001, personal communication). The respective regression coefficients have been estimated empirically from a number of MODIS nighttime analyses (J. Xiong and W. Barnes 2002, personal communication).

VIRS is a simplified five-channel version of MODIS (Barnes et al. 2000). The leaking energy on VIRS is 2–3 times larger compared to MODIS, due to a larger amplitude and the wider width of its secondary peak (C. Moeller 2001, personal communication), and VIRS bands 4 (10.8 μm) and 5 (11.9 μm) are not optimal to predict the leak signal because they are sensitive to much lower near-surface atmospheric layers. (Note that channel 3 at 3.8 μm is not used here because in the daytime it measures a complex mixture of reflected sun and emitted earth radiation.) To somewhat compensate for the dramatic difference between the weighting functions of the leak and window channels, the VIRS 5.2-μm leak peaks lower in the atmosphere, and includes a more significant contribution from the earth's surface compared to the MODIS leak at 5.3 μm, which extends to longer wavelengths with more water vapor absorption (C. Moeller 2001, personal communication). Also, the VIRS channel 4–5 difference, $R_4 - R_5$, is sensitive to the vertical gradient of water vapor in the lower atmosphere, which can be used to scale the near-surface window signals, R_4 and R_5, up to higher altitudes. However, the overall VIRS potential for accurate thermal leak correction remains low compared to MODIS.

Ignatov and Stowe (2000) derived a correction (hereafter, referred to as IS00) empirically from a limited amount of all-sky nighttime ($100° \leq \theta_o \leq 170°$) data for 1 h (Hr = 1) on 1 May 1998, and tested it by applying it to a daytime portion ($\theta_o \leq 60°$) of Hr = 20 on the same day. The false signal in channel 2 was parameterized as a linear function of R_4 and R_5, and a quadratic function of view angle θ. The effect of the IS00 correction on nighttime radiances for Hr = 1, and on aerosol retrievals from daytime data for Hr = 20 on 1 May 1998, was documented in Ignatov and Stowe (2000, see their Figs. 4 and 5). In 1999, the IS00 correction was applied to VIRS data to produce the TRMM SSF edition 1 dataset. However, it soon became apparent that the IS00 correction performs unstably over time.

W. Barnes [NASA Goddard Space Flight Center (GSFC)] and L. Stowe [National Oceanic and Atmospheric Administration/National Environmental Satellite, Data, and Information Service (NOAA/NESDIS)] worked together to find a quick fix. On a limited dataset, they observed a correlation of the IS00 residual in channel 2 with R_4, only when the temperature of the VIRS detector exceeded 113 K (W. Barnes and L. Stowe 2001, personal communication). A simple adjustment (hereafter referred to as BS01) was thus developed and applied at the top of the IS00 correction while producing the TRMM SSF edition 2A dataset in June 2001.

Comprehensive self-consistency checks of VIRS aerosol retrievals (not presented here) using the methodology of Ignatov and Stowe (2000, 2002) clearly indicate that τ_2 and α remain problematic in both editions of SSF. This triggered more in-depth analyses of the original, and IS00- and (IS00 + BS01)-corrected nighttime data. Their results are documented below in section 3. All analyses consistently and unambiguously point to the conclusion that the thermal leak remains a major source of error in channel 2, seriously limiting its aerosol information content. A more accurate correction is thus needed.

A new correction is formulated in section 4 and tested with two representative 9-day subsets of TRMM SSF data: one from 4 to 12 February, and the other from 2 to 10 April 1998. It effectively eliminates the systematic biases, and significantly improves the shape, and reduces the rmse of the residual. The time, geography,

R_4, R_5, and θ trends, clearly traced in the original nighttime signal in channel 2, and in the IS00 and (IS00 + BS01) residuals, are also minimized. These improvements result from three new developments: 1) explicit accounting for the temporal instability in the false signal (as opposed to an assumption of its stability over time in IS00, or its correlation with the VIRS detector temperature in BS01); 2) using empirical orthogonal functions (EOFs), or principal component analysis (PCA), to fit the false signal as a function of R_4, R_5, and θ (in place of formerly used less accurate regressions); and 3) using the clear-sky ocean subset (rather than the all-sky full set used in the previous corrections), to emphasize the domain of the radiances used for aerosol retrievals. The price to pay for the improved accuracy is a time-consuming preprocessing, which requires three passes through the nighttime data to consecutively derive three sets of time-dependent loadings (or principal components, PCs) on the respective EOFs. In addition to an improved correction in channel 2, which is the major problem with aerosol retrievals from VIRS, we also suggest that a much smaller spurious signal of unknown origin in VIRS channel 1, which has been neglected in the past, be corrected as well.

The parameterizations developed from nighttime data in this study force the residual of the correction to be centered at zero. However, two mechanisms may potentially contribute additional systematic errors while applying these parameterizations to correct daytime radiances. First, the VIRS nighttime and daytime clear-sky identifications differ: one uses only three thermal IR channels as opposed to the other, which uses all five (Trepte et al. 1999). This difference, if it exists, can be further amplified or offset by the effect of the diurnal cycle in thermal radiances. Both effects can be quantified only by simultaneous use of daytime and nighttime data, and are not addressed in this study, which uses nighttime data only.

This study contributes toward an improvement of the VIRS data quality, with the ultimate objective of more fully exploring the VIRS aerosol information potential. Its results are deemed to be useful for both aerosol remote sensing scientists and instrument developers. Design, and the actual instrument performance, must be taken into account in the development of aerosol algorithm, as these factors may cause significant errors in the derived aerosol product and, thus, seriously limit its information content. Analyses of the VIRS radiometric anomaly may also be insightful for instrument designers, to help better understand and avoid this kind of problem with future instruments.

2. VIRS clear-sky nighttime data on TRMM SSF

This study uses nighttime clear-sky statistics of VIRS radiances in channels $i = 1, 2$ and $i = 4, 5$ over the ocean, mapped into CERES footprints. Night is defined as the time when TRMM is at least 10° below the horizon (sun angle $100° \leq \theta_o \leq 170°$). In reflectance channels 1 and 2, a zero signal would be observed on the dark side of the earth if those channels performed as expected. However, both channels measure nonzero radiances at night. Herein, these signals are referred to as spurious, or false, to emphasize the fact that their presence is unwanted and complicates the use of daytime data for product applications such as aerosol retrievals and cloud identification. The nature of the false signal in channel 2 is well understood whereas the origin of a much smaller nighttime signal in channel 1 is less clear.

On the SSF, VIRS radiances R_i are reported in units of W m^{-2} sr^{-1} μm^{-1}. In channels 4 and 5, R_4 and R_5 are used in this study as they are given on the SSF. In channels 1 and 2, R_1 and R_2 have been converted to albedo units by normalizing to overhead sun as $A_i(\%) = 100\% \times R_i/F_i$, where $F_1 = 531.7$ and $F_2 = 78.3$ W m^{-2} sr^{-1} μm^{-1} are solar fluxes in the respective channels. Although there is no ''overhead sun'' at night, the definition of ''dark'' albedo, A_i, offers an easy way to estimate the respective error in AOD through a simple relationship $\tau_i \sim C \times A_i(\%)$ based on a simplified treatment of the radiative transfer equation (e.g., Ignatov and Stowe 2000; Ignatov 2002). The conversion factor C does not depend upon channel and typically ranges from 0.10 to 0.20, due to a variable sun-view geometry. For the remainder of this paper, an average value of $C \sim 0.15$ is adopted. More accurate estimates of τ sensitivity, and its effect on the Ångström exponent, will be given elsewhere while testing the correction with daytime data.

In the TRMM SSF edition 1 (1999), only the daytime portion of data (used in cloud detection and aerosol retrievals) was IS00 corrected, whereas nighttime measurements were left intact. In edition 2 (2001), however, the BS01 adjustment was applied to both day- and nighttime data. The adjustment was ''on'' when the VIRS detector temperature was above $T_D > 113$ K. The T_D parameter was not saved on the SSF, and there is no easy way to recover the original VIRS channel 2 radiances from the SSF edition 2 data. This study uses edition 1 data, which allows interpretation of the EOFs and PCs derived in section 4 as pertinent to the actual performance of the VIRS instrument rather than to the alterations introduced by the BS01 adjustment. (Edition 2 data were used only once while testing the effect of the BS01 adjustment in section 3.) Note, however, that if a decision is made to implement the proposed correction with the TRMM SSF, then the most recent edition 2 must be used. As a result, the intermediate derivations of the correction (EOFs and PCs) may change but not its accuracy.

The datasets used in this study are for the two 9-day periods, from 4 to 12 February, and 2 to 10 April 1998 (hereafter referred to as Feb98 and Apr98, respectively). Each includes 216 hourly SSF files collected from 142 orbits. In edition 1, the nighttime portion contains $N =$

4 667 624 (Feb98) and $N = 6\ 358\ 737$ (Apr98) CERES footprints (SSF pixels) with valid VIRS clear-sky statistics over ocean. In edition 2, the respective statistics are $N = 4\ 858\ 507$ and $N = 6\ 557\ 632$. Note that the increase by $\Delta N = +190\ 883$ (+4.1%; Feb98) and $\Delta N = +190\ 883$ (+3.1%; Apr98) from edition 1 to edition 2 is due to minor developments and adjustments in the cloud screening procedure by Trepte et al. (1999).

3. False signals and residuals of different corrections

a. Channel 2

Histograms of the original A_2 for the two datasets are shown in the first row of Fig. 1. They suggest a few observations.

1) The average false signal is $A_2 \sim 0.73\%\text{–}0.87\%$, equivalent to a positive AOD bias of $\tau_2 \sim +0.11$ to $+0.13$. This error exceeds the typical $\tau_2 \sim +0.10$ over oceans (cf. Ignatov and Stowe 2000).
2) The false signal varies from one dataset to the other. The average difference ("Feb98 minus Apr98") is $\Delta A_2 \sim +0.15\%$, equivalent to an AOD discontinuity of $\Delta \tau_2 \sim +0.02$ ($\sim$20% of typical τ_2).
3) The false signal varies within each dataset. Rmsd is $\sigma_{A2} \sim 0.10\%\text{–}0.13\%$, equivalent to $\sigma_{\tau 2} \sim 0.02$. The range of variability within each dataset defined as $\max(A_2) - \min(A_2)$ is $\sim$0.6%–0.8%, or $\pm$(0.3–0.4)%, equivalent to $\delta\tau_2 \sim \pm(0.04\text{–}0.06)$ ($\pm$40% to $\pm$60% of typical τ_2).

It is thus clear that without a correction, aerosol retrievals in channel 2 are meaningless. Ignatov and Stowe (2000) arrived at this conclusion and attempted to fix the problem. They came up with the following equation to predict A_2 as a function of R_4, DR $= R_4 - R_5$, and θ:

$$A_2 = A_0 + A_R R_4 + A_{DR}(R_4 - R_5) + A_{\theta 1}\theta + A_{\theta 2}\theta^2. \quad (1)$$

The regression coefficients were derived empirically using only 1-h (Hr = 1) of all-sky *pixel-level* (as opposed to the clear-sky *SSF statistics* over ocean, used in this study) VIRS data collected on 1 May 1998. Residuals of the IS00 correction are shown in the second row of Fig. 1. The correction does a reasonable job in Feb98, reducing bias down to $A_2 \sim +2 \times 10^{-3}\%$ ($\tau_2 \sim +3 \times 10^{-4}$). However, in Apr98 it leaves a negative bias of $A_2 \sim -0.137\%$ ($\tau_2 \sim -2 \times 10^{-2}$). Rmsd is reduced by $\sim$1/3 in both datasets, down to $\sigma_{A2} \sim$0.067%– 0.086% [$\sigma_{\tau 2} \sim (1.0\text{–}1.3)10^{-2}$]. The above estimates suggest, in particular, that in the SSF edition 1, produced with the IS00 correction, τ_2 is biased low by $\sim$−0.02 in Apr98. In Feb98, the bias is negligible.

The BS01 (third row of Fig. 1) rightly identifies the need for further adjustment in Apr98 but not in Feb98. The decision-making based on the VIRS detector temperature thus appears trustworthy, at least in the analyzed data, and may indirectly support the hypothesis of VIRS instability as the major cause for the IS00 failure in Apr98. It may further suggest that W. Barnes and L. Stowe (2001, personal communication) have correctly identified the major indicator and predictor of this instability—the temperature of the VIRS detector. Not only does the BS01 rightly identify whether the correction is needed, but it also correctly predicts its sign, shifting the Apr98 A_2 up in the right direction. However, quantitatively the adjustment is exaggerated, ending up with a positive bias of $A_2 \sim +0.162\%$ ($\tau_2 \sim +2 \times 10^{-2}$) in the (IS00 + BS01) residual in SSF edition 2, with almost unchanged rmsd, compared to the IS00 residual. In Feb98, the bias remains negligible.

The Barnes–Stowe (2001, personal communication) philosophy of normalizing VIRS data to a common detector temperature is based on a clear physical premise and appears to work in practice, at least qualitatively. Further quantitative improvements to it are possible through adjustments to the parameters of the correction using a more Gaussian shape of the residual, and minimization of its bias and rmsd, as the criteria. However, this approach appears impractical with the current SSF data, from which the VIRS detector temperature is missing. Therefore, a pure statistical procedure based solely on SSF data was tested as an alternative to the former physical corrections by Ignatov and Stowe (2000) and W. Barnes and L. Stowe (2001, personal communication). This procedure is described in the next section, but its results are preliminarily shown here, side by side with the former corrections, to allow better appreciation of the proposed improvement.

The bottom panel of Fig. 1 shows histograms of the residual of the proposed correction. In both datasets the bias does not exceed $A_2 \sim +0.006\%$ (equivalent to $\tau_2 \sim +2 \times 10^{-3}$). The rmsd is $\sigma_{A2} \leq 0.055\%$ (equivalent to $\sigma_{\tau 2} \sim 8 \times 10^{-3}$), a $\sim$55% improvement from the original data, and $\sim$33% from either the IS00 or (IS00 + BS01) corrections. The shape of the residual is symmetric with respect to zero and close to Gaussian.

The top rows of Figs. 2–4 plot histograms of θ, R_4, and DR for Feb98. Note that the VIRS view angle, reported from 0°–48° on the SSF, was redefined for this study in the interval from −48° to +48° based on the relative azimuth angle with respect to the sun so that positive θ values correspond to the solar and negative to the antisolar directions. This new definition allows one to resolve the asymmetry with respect to nadir observed in all channels (cf. Figs. 2b, 7a2, and 8b), whose nature is not fully understood. An angle range of $\theta = -48°$ to $+48°$ is relatively uniformly filled in with the data (the cause for the sawlike structure is not immediately clear). A histogram of the clear-sky ocean R_4 reveals a peak at $\sim$8.5 W m^{-2} sr^{-1} μm^{-1}, but there is a long cold tail reaching down to 3–4 W m^{-2} sr^{-1} μm^{-1}, supposedly due to the effect of residual cloud. The DR histogram peaks at $\sim$0.7 W m^{-2} sr^{-1} μm^{-1}, and also deviates from a Gaussian shape.
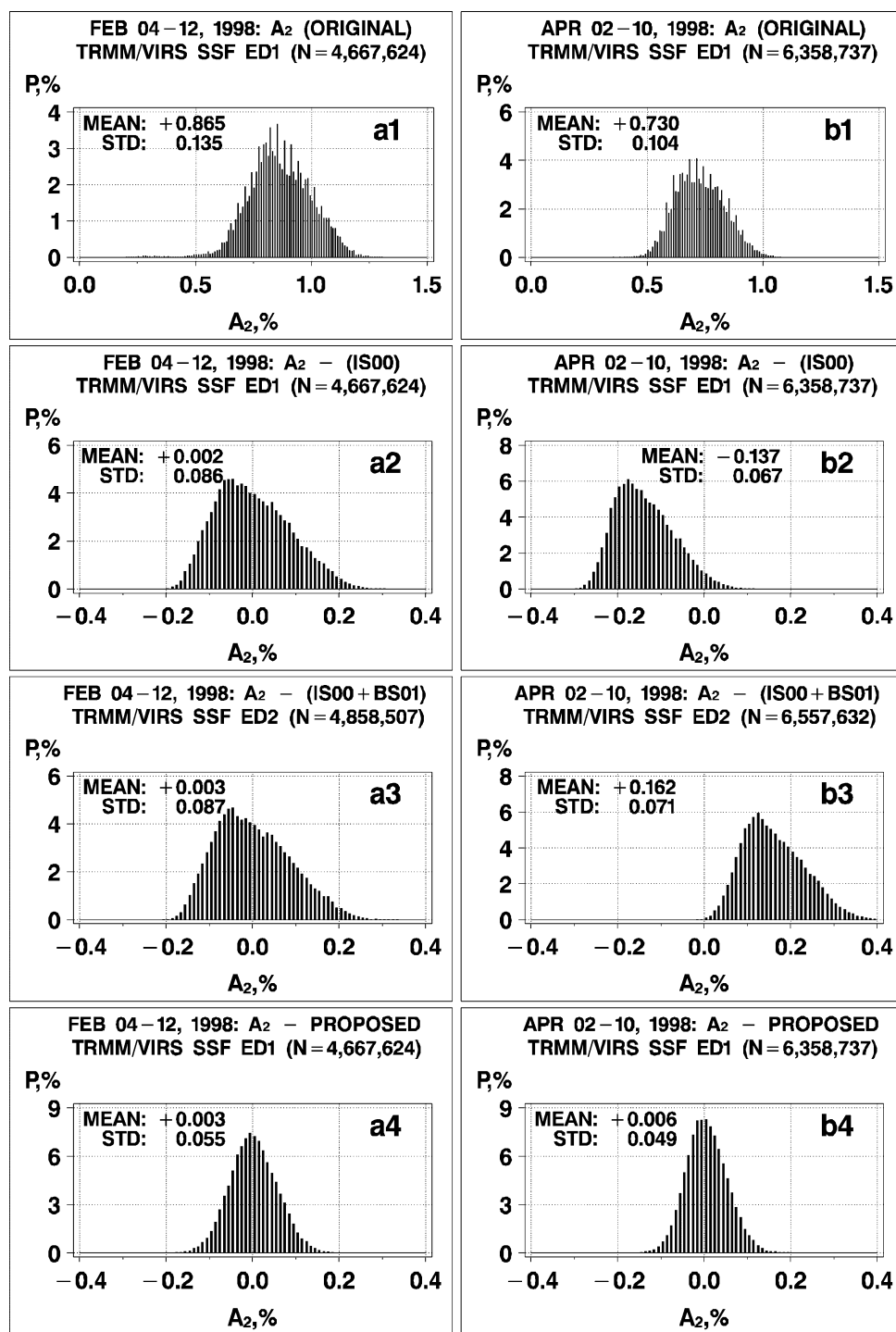
The next four lines in Figs. 2–4 plot the respective

FIG. 1. (first row) Histograms of original A_2 (needles centered on $\Delta A_2 = 0.01\%$ bins) for (a) Feb98 and (b) Apr98, and residuals of (second row) IS00, (third row) (IS00 + BS01), and (fourth row) proposed corrections.

trends in the original A_2, and residuals of the three corrections. Recall that the IS00 correction was specifically designed to fit the A_2 as a function of these three parameters. The quadratic fit in θ appears to work reasonably well, but the R_4 and DR trends are clearly traced in the IS00 residual. The reason is that rather complicated R_4 and DR dependencies in the original data (Figs. 3b and 4b) were simplistically approximated with linear
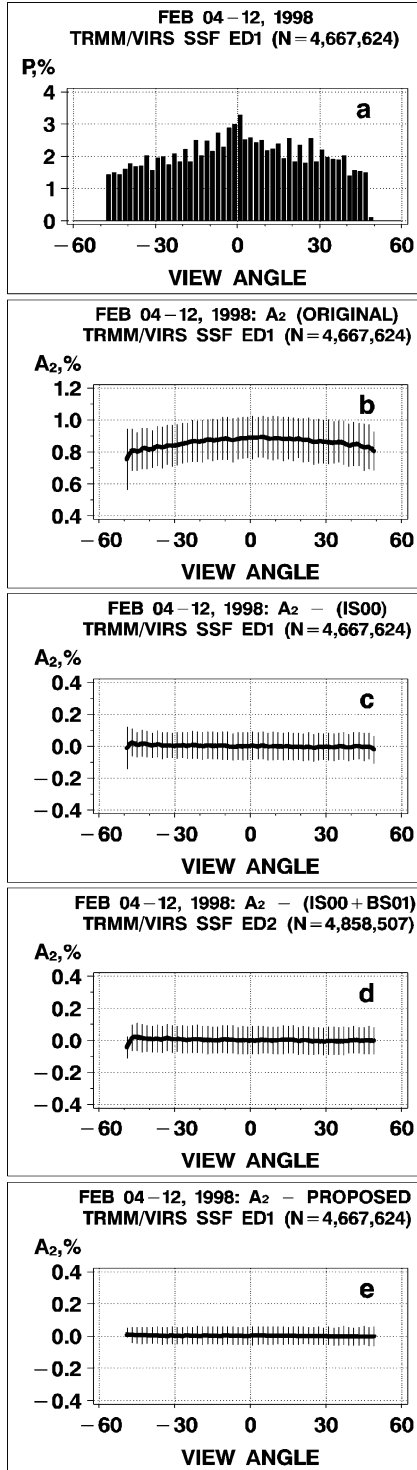
FIG. 2. Feb98: (a) histograms of view angle (needles centered on $\Delta\theta = 2°$ bins), and (2–5) average view angle trends in A_2 for (b) original; and residuals of (c) IS00, (d) (IS00 + BS01), and (e) proposed corrections. Whiskers are at the respective (bin specific) STDs.
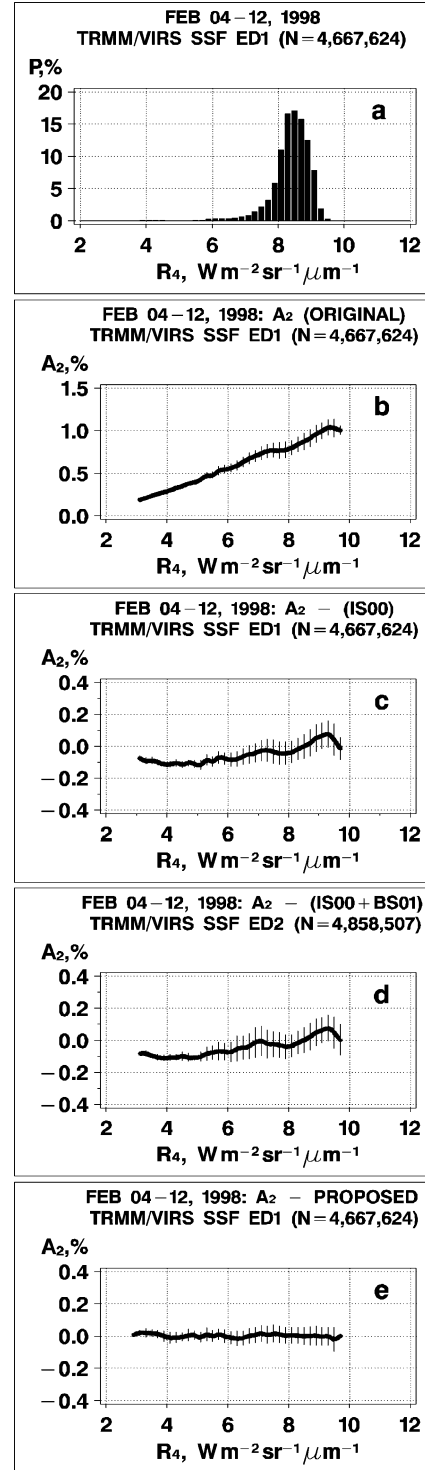
FIG. 3. Same as in Fig. 2 but for R_4 (needles centered on $\Delta R_4 = 0.2$ W m^{-2} sr^{-1} μm^{-1} bins).
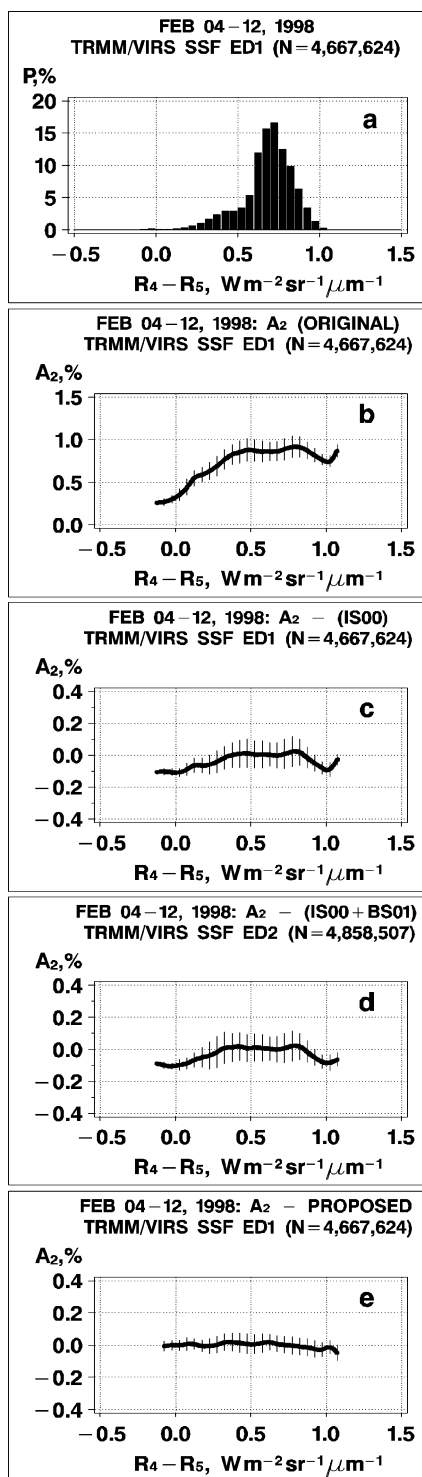
FIG. 4. Same as in Fig. 2 but for DR = $R_4 - R_5$ (needles centered on ΔDR = 0.05 W m^{-2} sr^{-1} μm^{-1} bins).
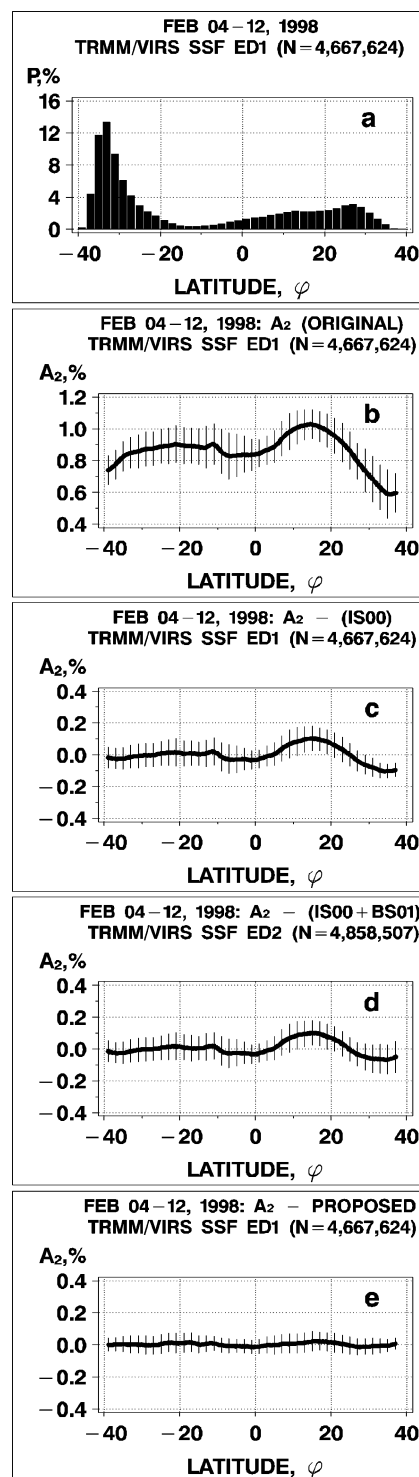

FIG. 5. Same as in Fig. 2 but for latitude λ (needles centered on $\Delta\lambda = 2°$ bins).

functions. The problems traced in the IS00 residual are not resolved by the BS01 adjustment either, but they are greatly alleviated by the proposed correction.

Figures 5 and 6 additionally show latitudinal (φ) and temporal (t) trends in A_2, along with their respective histograms. The spurious spatiotemporal variability with different scales, clearly traced in the original data and in the residuals of the past two corrections, is no-

ticeably reduced by the proposed correction. Note that the temporal variability is explicitly accounted for in the correction algorithm and therefore its removal is expected, but the spatial variability is not. Removal of the latitudinal trend is thus an additional independent indicator of the high performance of the correction.

b. Channel 1

Figure 7a1 shows a histogram of the "dark albedo" in channel 1 in Feb98. Average A_1 is $\sim 2.7 \times 10^{-2}$% (in Apr98, $A_1 \sim 3.7 \times 10^{-2}$%; not shown), the rmsd within each dataset is $\sigma_{A1} \leq 0.013$%, and the difference between the Feb98 and Apr98 datasets is $\Delta A_1 \sim 1 \times 10^{-2}$%. These are equivalent to a high bias of $\tau_1 \sim +5 \times 10^{-3}$, rmsd $\sigma_{\tau1} \sim 2 \times 10^{-3}$, and $\Delta \tau_1 \sim 1.5 \times 10^{-3}$, respectively.

The origin of the false signal in channel 1 is unclear but its distinct θ, latitude, time (Figs. 7a2–4), and negligible R_4 and DR trends (not shown) suggest that its nature is different from that in channel 2. An increase in A_1 toward the antisolar side of the orbit may suggest that a solar signal reflected from VIRS is the cause. From a practical perspective, however, its amplitude is an order of magnitude smaller compared to A_2. Relating the above errors to a typical $\tau_1 \sim 0.15$ (e.g., Ignatov and Stowe 2000, 2002), one obtains that the spurious signal contributes only $\sim$3% of the typical τ_1. This is a small error, and it can be neglected as was done in the past. However, a relatively inexpensive and straightforward manipulation to channel 1 data (much simpler than in channel 2) seems to improve its quality. The right panel of Fig. 7 shows the residual of the proposed correction. Bias is removed, the histogram in Fig. 7b1 is centered at zero, it is more symmetric, and it is closer to a Gaussian shape. The rmsd is reduced more than 2 times, down to $\sigma_{A1} \sim 0.005$%, equivalent to a residual AOD error of $\sigma_{\tau1} \sim 8 \times 10^{-4}$. The residual reveals no trend with either view angle, latitude, or time (Figs. 7b2–4), or thermal channels (not shown).

4. Proposed correction

a. Principles of the correction

The empirical correlations of A_2 with θ, R_4, and R_5 (examples for Feb98 shown in Figs. 2b, 3b, and 4b, respectively) are more complex than the simplistic linear/quadratic approximations with Eq. (1) used in the IS00. Figure 6b further suggests that the false signal reveals some time trends. It is therefore proposed that $A_2(R_4, R_5, \theta; t)$ be *tabulated* (rather than approximated *analytically*) as a function of (θ, R_4, R_5) and time t. Temporal resolution of the correction is limited to one TRMM orbit, because the tabulations derived from its dark segment are assumed to hold over its sunlit part. A higher-frequency (*suborbital*) temporal variability, if it exists, would contribute to the residual error of the correction.
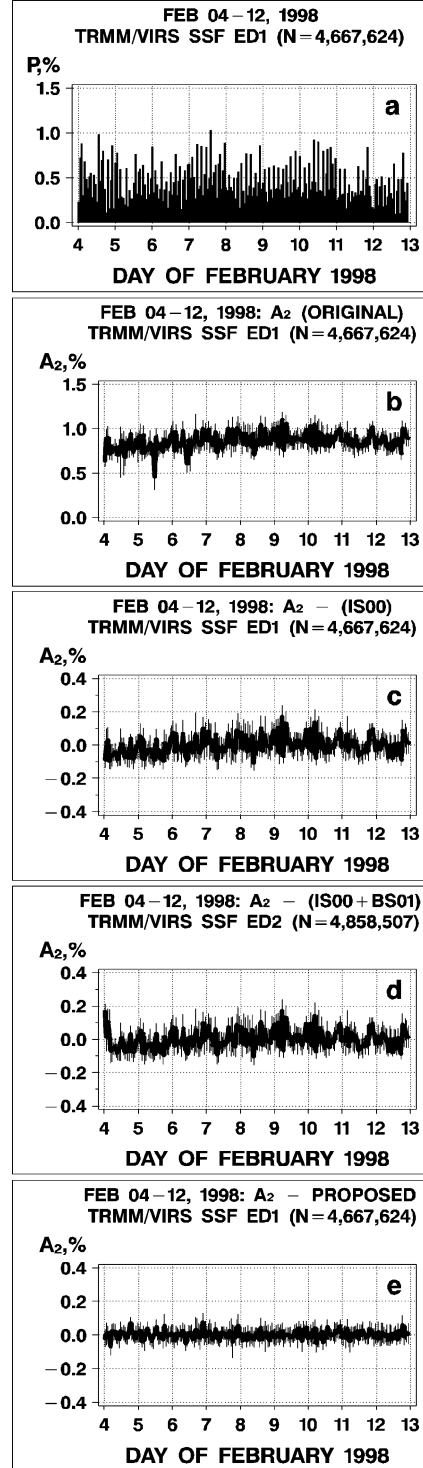

FIG. 6. Same as in Fig. 2 but for time t (needles centered on $\Delta t = 1$ h bins).

The above considerations suggest the following structure of the correction algorithm. First, an average dependence of $A_2(\theta, R_4, R_5)$ is estimated from the nighttime segment of an orbit, by averaging all A_2 values
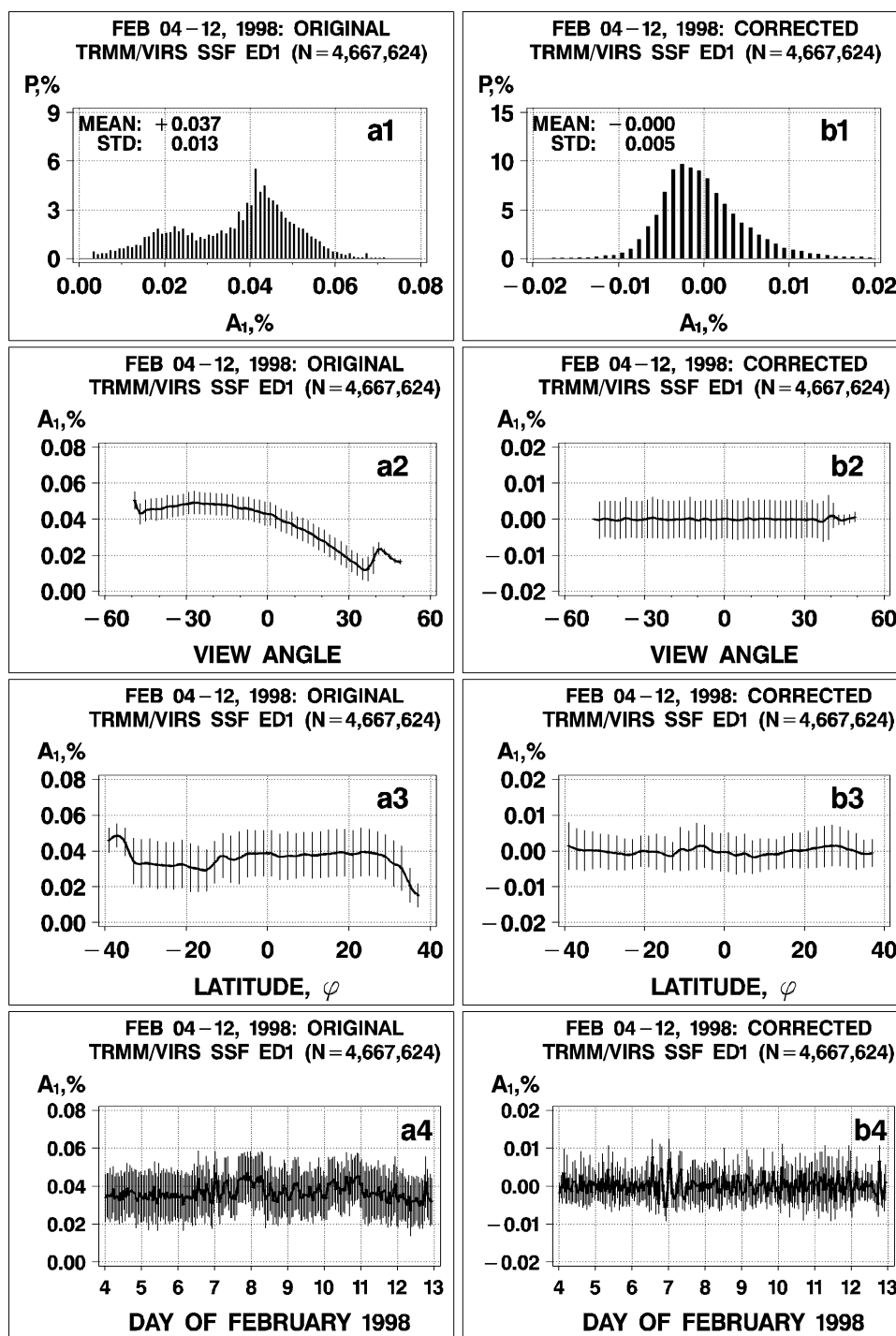
FIG. 7. (1) Histograms of A_1 (needles centered on $\Delta A_1 = 10^{-3}\%$ bins) and (2–4) trends in A_1 for Feb98: (a) original and (b) corrected. Whiskers are at the respective (bin specific) STDs.

within specially chosen (θ, R_4, R_5) bins. This three-dimensional look-up table (LUT) is then applied to the daytime portion of the same orbit to predict A_2 as a function of measured (θ, R_4, R_5) for each SSF footprint. Finally, the predicted A_2 is subtracted from the VIRS daytime albedo measurement. Note that the LUTs of

$A_2(\theta, R_4, R_5)$ are estimated and applied on an orbit-by-orbit basis.

Practical implementation of this procedure is not straightforward for a number of reasons: 1) one should calculate and keep available as many three-dimensional LUTs for as many orbits as are to be processed. For

instance, each of the two 9-day datasets used here consists of 142 orbits, and full TRMM data record from 1998 on would thus contain more than 30 000 orbits. Processing difficulties increase with the size of the satellite data record. 2) Some bins of the three-dimensional (θ, R_4, R_5) space may be missing at night but may be present during daytime, due to different sampling; filling in these missing bins may require interpolation or extrapolation; 3) certain bins, although filled in, may reveal nonsmooth R_4, R_5, and θ dependencies in A_2, due to, for example, insufficient sampling; and 4) the continuity/smoothness between different orbits is also not automatically ensured, as the LUTs for different orbits are estimated independently.

The following approach is proposed to resolve these issues.

1) It is postulated that one four-dimensional analysis of A_2 (θ, R_4, R_5; t) can be done in three consecutive two-dimensional steps: $A_2(\theta; t)$, $A_2(R_4; t)$, and $A_2(R_5; t)$. At the first step, the θt dependence in A_2 is parameterized (having all measurements with different R_4 and R_5 combined together) and removed from the data. This step is referred to as the θt correction and is described in section 4c. In the second step, the $R_4 t$ dependence is analyzed (having combined all the θt residuals with different θs and R_5s) and removed. This step is referred to as the $R_4 t$ correction and is described in section 4d. Finally, the $R_5 t$ dependence is analyzed (having combined all the $R_4 t$ residuals with different θs and R_4s) and removed. This step is referred to as the $R_5 t$ correction and is described in section 4e. Note that the physical interpretation of each step is not as straightforward as its name may suggest, due to the correlations between the three factors (the strongest being between R_4 and R_5). We suggest that the procedure should be rather viewed as a sequential removal of the three A_2 components, respectively, correlated to the first factor, then to the part of the second factor uncorrelated with the first factor, and then to that part of the third factor uncorrelated with the former two. Note that the three components are not necessarily ranked in the order of their relative contribution to A_2.

2) One orbit is considered a time bin, $\Delta t = 1$ orbit. For the sake of either θt, $R_4 t$, or $R_5 t$ analyses, all night data within an orbit are averaged out within discrete bins of a respective parameter: $\Delta\theta = 2°$, $\Delta R_4 = 0.2$ W m^{-2} sr^{-1} μm^{-1}, and $\Delta R_5 = 0.2$ W m^{-2} sr^{-1} μm^{-1}. Each such orbital-average one-dimensional dependence of $A_2(\theta)$, $A_2(R_4)$, and $A_2(R_5)$ (averaging is done over ~40 000 individual SSF pixels) is called a vector. This study analyzes a total of 284 θ, R_4, and R_5 vectors (142 in Feb98, and 142 in Apr98).

3) To represent each vector in the most natural and economic way, a formalism of EOFs, or PCA, is used. Each θ, R_4, or R_5 vector is represented as a linear combination of an average vector, and a few respective EOF vectors, which depend upon either θ, R_4, or R_5, but not time. In contrast, the loadings on the respective EOFs, called PCs, depend upon time but not θ, R_4, or R_5. This is the way to separate the two variables in the respective two-dimensional analyses. The EOF/PCA approach provides additional advantages of smoothing the θ, R_4, and R_5 dependencies, by rectifying signal from noise, and filling in the missing bins. Note that a large part of the temporal variability in the false signals is expected to be removed at the first stage of temporal analyses, which happens to be the θt correction. If this is the case, then the orbit-to-orbit variability in the R_4 and R_5 vectors should be small, and the $R_4 t$ and $R_5 t$ EOF analyses unnecessary. Analyses in sections 4c and 4d below confirm that approximating the 284 orbital R_4 and R_5 vectors with the respective average vectors is, indeed, sufficiently accurate. The EOF/PC additions do not improve this accuracy significantly, nor can they deteriorate it. Keeping three EOFs consistently in all analyses allows one to check this intuitive expectation.

4) Finally, the PCs are plotted as a function of time and examined if temporally smooth and coherent. Residual noise in the time series is filtered out with a 7-orbit ($\pm$3) moving average, to ensure their temporal coherence, and applicability of the nighttime-derived parameterizations during daytime.

b. Three types of statistics

Three types of statistics are used in this section. The first two are intermediate results of derivation of the correction procedure, and are given here for completeness and illustration purposes only. The third statistics characterizes the actual performance and accuracy of the parameterization. This section attempts to clearly differentiate between them to avoid confusion.

Type 1 (interorbital variability/no smoothing in time): The average (Figs. 8b, 11b, 14b) and STD (Figs. 8c, 11c, 14c) vectors are calculated over the 284 orbital vectors. STD vectors can be viewed as the residual rmse of approximating the 284 individual vectors with the respective average vectors (i.e., they do not include a *suborbital* variability), to be reduced through the EOF/PC analyses. The degree of the EOF/PCA improvement is quantitatively characterized by the respective percent explained variance (PEV) η superimposed in the EOF graphs (Figs. 9a, 12a, and 15a). The corresponding PCs are shown in (Figs. 9c, 12c, and 15c) with circles. For instance, if the STD over the 284 vectors was $\sigma = 1$ (arbitrary unit), and the first k EOFs explain 99% ($\eta = 0.99$) of this variance, then the residual rmse of approximating with k EOFs is $\sigma/\sqrt{(1-\eta)} = 0.1$. Note that the bias of approximating the 284 orbital vectors

TABLE 1. Bias and rmse in the original $N = 11\,026\,361$ *individual* SSF pixels, and residuals of different approximations.

Feb 98 Apr98		Original	Avg	$\cdots$+EOF1	$\cdots$+EOF2	$\cdots$+EOF3
θt correction	A_1 (%)	(+0.032)	(−0.000)	(+0.000)	(+0.000)	(+0.000)
		1.24×10^{-2}	8.40×10^{-3}	5.38×10^{-3}	5.24×10^{-3}	5.24×10^{-3}
	A_2 (%)	(+0.787)	(−0.009)	(+0.001)	(+0.001)	(+0.001)
		1.36×10^{-1}	1.34×10^{-1}	1.10×10^{-1}	1.09×10^{-1}	1.09×10^{-1}
	R_4, (W m^{-2} sr^{-1} μm^{-1})	(+8.474)	(+0.009)	(+0.006)	(+0.005)	(+0.005)
		5.61×10^{-1}	5.58×10^{-1}	5.18×10^{-1}	5.17×10^{-1}	5.17×10^{-1}
	R_5, (W m^{-2} sr^{-1} μm^{-1})	(+7.750)	(+0.010)	(+0.006)	(+0.005)	(+0.005)
		4.43×10^{-1}	4.39×10^{-1}	4.12×10^{-1}	4.11×10^{-1}	4.10×10^{-1}
$R_4 t$ correction	A_2 (%)	(+0.001)	(+0.002)	(+0.002)	(+0.002)	(+0.003)
		1.09×10^{-1}	8.71×10^{-2}	8.43×10^{-2}	8.36×10^{-2}	8.36×10^{-2}
	R_5, (W m^{-2} sr^{-1} μm^{-1})	(+0.005)	(+0.001)	(+0.000)	(+0.001)	(+0.001)
		4.10×10^{-1}	9.22×10^{-2}	9.12×10^{-2}	9.01×10^{-2}	8.98×10^{-2}
$R_5 t$ correction	A_2 (%)	(+0.003)	(+0.005)	(+0.005)	(+0.005)	(+0.005)
		8.36×10^{-2}	5.25×10^{-2}	5.24×10^{-2}	5.19×10^{-2}	5.18×10^{-2}

with an average vector, in combination with any number of EOFs, is zero by definition.

Type 2 (interorbital variability/smoothing in time): To ensure the applicability of the nighttime-derived PCs (circles in Figs. 9c, 12c, and 15c) during daytime, they have been smoothed out in time with a ±3 orbit moving average filter (dashed lines) to rectify the temporally coherent component from noise (deviation of circles from the dashed lines). Note that the temporal smoothing of PCs increases the rmse's of the EOF residual (shown in Figs. 9b, 12b, and 15b) from those predicted from the respective PEVs (but it does not affect the EOFs themselves), and may result in a small deviation of the bias from zero.

Type 3 (inter- and intraorbital variability/smoothing in time): The actual performance of the correction, however, is measured by how well the average vectors and EOFs with temporally smoothed PCs derived from only 284 orbital vectors predict the radiances in each *individual* SSF footprint (recall that there are $N = 11\,026\,361$ SSF pixels in the combined Feb98 + Apr98 dataset). The respective bias and rmse statistics are listed in Table 1 and are superimposed in Figs. 1a4, 1b4, and 7b1. Small deviations of biases from zero in the four rightmost columns of Table 1 are expected, due to the above-mentioned minor imbalance of the temporally smoothed PCs, and due to the procedure of estimating the average vectors. Recall that the average vector is calculated by averaging of 284 orbital vectors, each of which is itself a result of averaging the *individual* SSF footprints within an orbit. Result of this two-step averaging may differ from a direct averaging over of the $N = 11\,026\,361$ *individual* SSF footprints. Type-3 rmse's are obviously larger than their respective type-1 and -2 counterparts, derived from only 284 vectors because now they include a *suborbital* variability (in addition to the *interorbital* variability suppressed by aggregating the $N = 11\,026\,361$ *individual* SSF pixels into 284 orbital vectors used in the EOF analysis).

c. View angle and time (θt) correction

We begin with the analyses and removal of the θt dependence from the dark albedos A_1 and A_2. Simultaneously, R_4 and R_5 are also θt-corrected to avoid propagation of their θt trends back into the A_2 residual when it is correlated against the thermal radiances in the next two stages of analysis.

Type-1 statistics (interorbital variability/no temporal smoothing): Figure 8a shows three examples (out of 284) of the orbital $\boldsymbol{\theta}$ vectors in the four VIRS channels, and Figs. 8b and 8c plot their average and STD statistics over 284 orbits. The average limb darkening is asymmetric in every single channel. The thermal signals in channels 2 and 4–5 tend to be warmer on the solar side of the orbit ($\theta > 0$), whereas the channel 1 signal is brighter on the antisolar side ($\theta < 0$), suggesting that it may originate from a reflection of the solar radiation by some elements of the VIRS instrument toward its detector. In channel 2, the STD $\boldsymbol{\theta}$ vector is nearly symmetric. In channels 4 and 5, the variability is a factor of 2 larger on the solar side ($\theta \sim +48°$) than on the antisolar side ($\theta \sim -48°$), whereas in channel 1, the reverse is true.

Figure 9a shows the first three $\boldsymbol{\theta}$ EOFs in each channel, with the PEVs superimposed. The first $\boldsymbol{\theta}$ EOF explains from 89.1% to 96.3% of the variance, the first two EOFs from 96.6% to 99.7%, and the first three from 98.1% to 99.8%. The PEVs are smallest in channel 5, and progressively increase toward channel 1.

Type-2 statistics (interorbital variability/temporal smoothing): Figure 9b shows residual rmse's of approximating the 284 individual $\boldsymbol{\theta}$ vectors with ($\boldsymbol{\theta}$ average + three $\boldsymbol{\theta}$ EOFs) and temporally smoothed PCs (dashes in Fig. 9c). The type-2 EOF residual is more uniformly distributed over the full range of the view angle, and $\sim$2–3 times reduced compared to the type-1 STD in Fig. 8c (which recall is an rmse of approximating the 284 individual $\boldsymbol{\theta}$ vectors with a $\boldsymbol{\theta}$ average
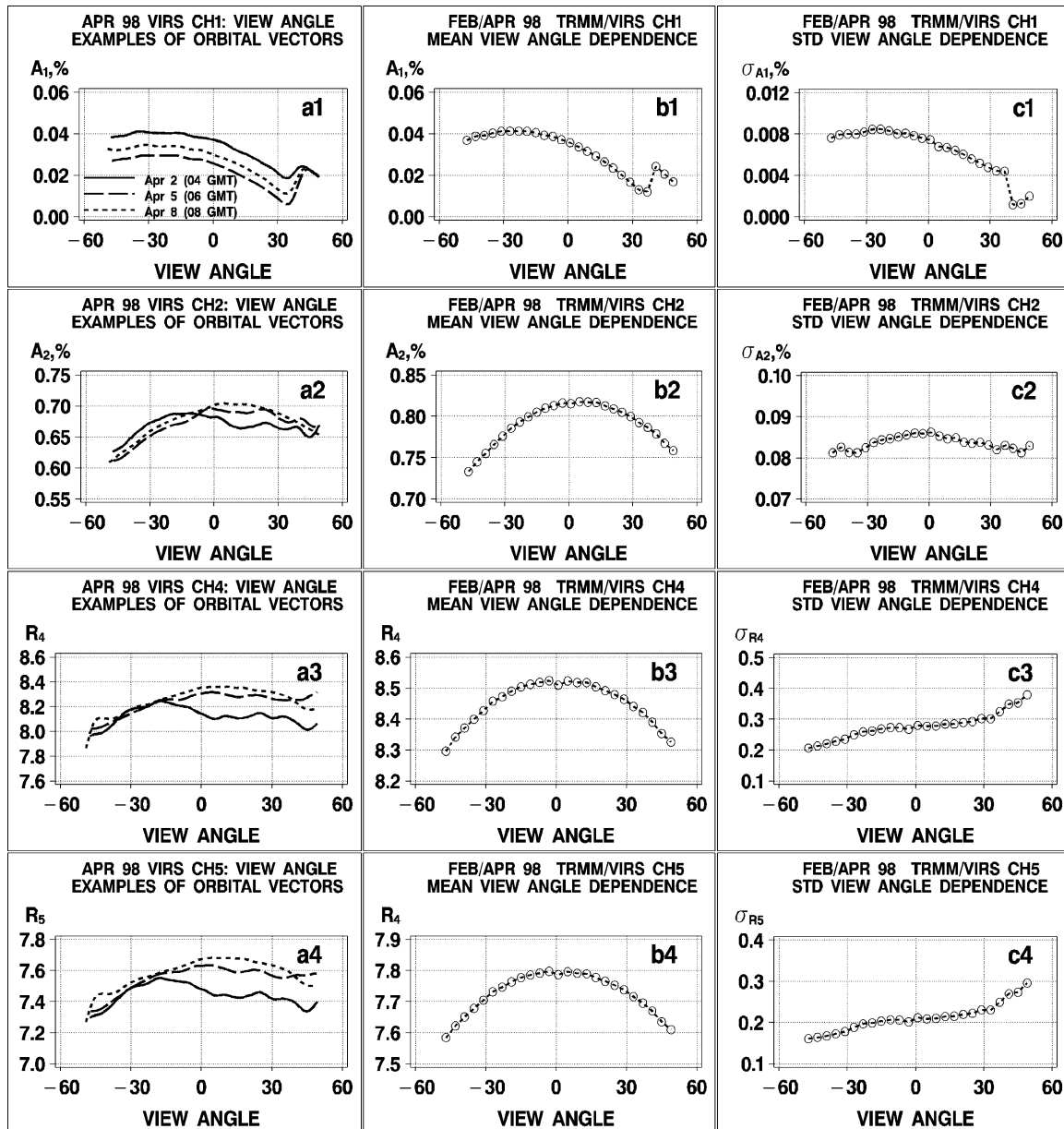
FIG. 8. Examples of (a) orbital mean θ vectors, (b) average, and (c) STD view angle dependencies over 284 (Feb98 + Apr98) orbital θ vectors in (top row) A_1, (second row) A_2, (third row) R_4, and (fourth row) R_5.

only). Note that the EOF improvement would be a factor of 7–22 (estimate from the PEVs in Fig. 9a) if the original PCs (circles in Fig. 9c) were pure coherent signals with no noise (in this case, the dashes would go exactly through the circles), and it would be zero if the PCs in Fig. 9c were pure "noise," with no coherent component. The actual improvement (a factor of ~2–3) falls in between these two ("optimistic" and "pessimistic") estimates.

Example time series of the θ PC1 for Feb98 (Fig. 9c) reveal a high degree of temporal coherence, at the top of which a noticeable noise component is superimposed.

For a correction during the daytime, the coherent signal component should be utilized whereas the noise component with frequencies higher than the orbital revolution should be filtered out. Rectifying signal from noise can be done in a number of different ways. Here, a 7-orbit (current orbit ± 3) moving averaging filter is used based on the fourth differences $1/21(-2, +3, +6, +7, +6, +3, -2)$ (e.g., Lanczos 1988). Results of its application, superimposed in Fig. 9c with dashed lines, suggest that the smoothed θ PCs become more coherent over time, compared to the more noisy original θ PCs. In channels 2 and 4–5, a quasi-daily cycle seems to
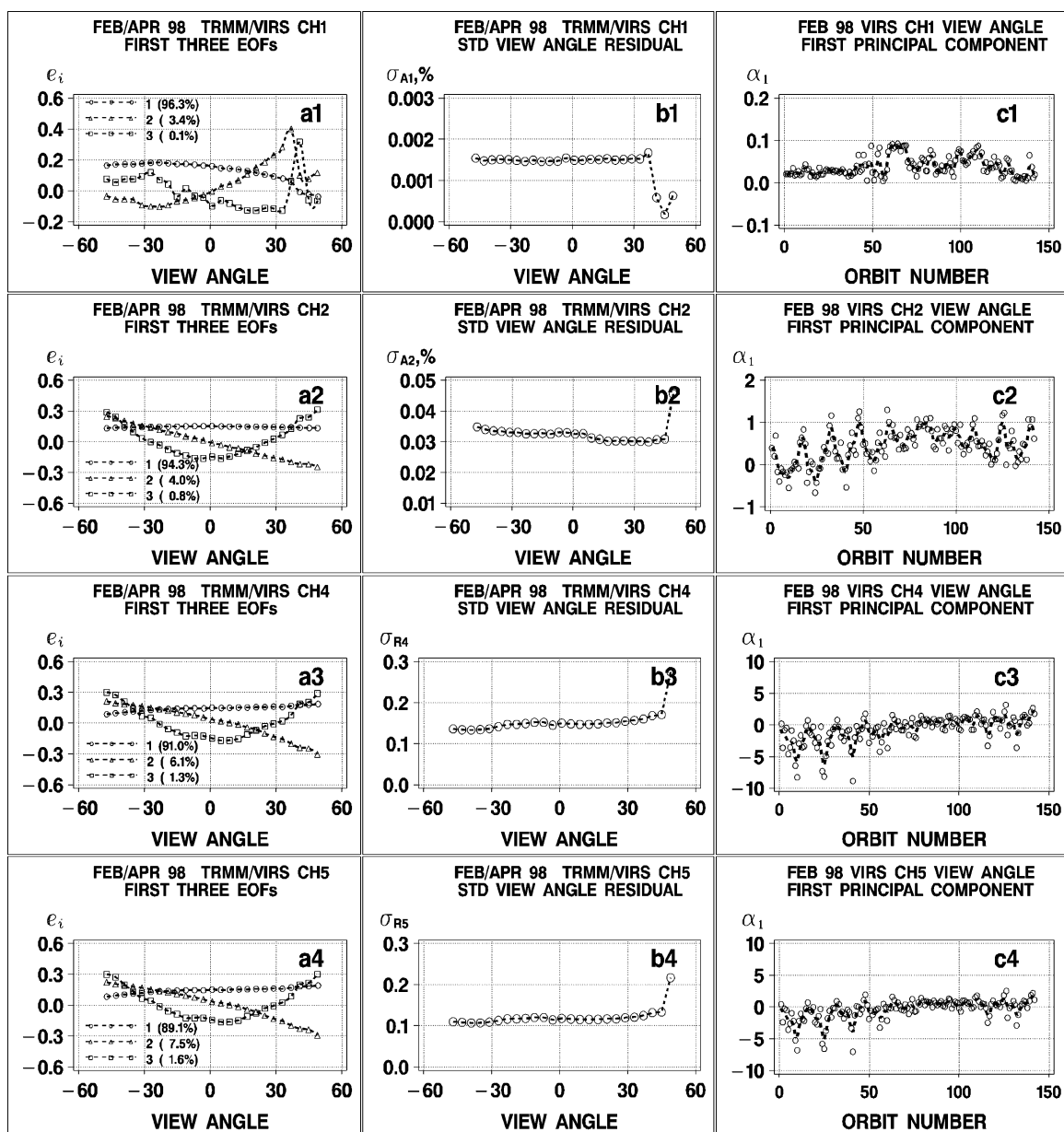
FIG. 9. (a) The **θ** EOFs, with PEV superimposed, (b) residual rmsd's (approximation with three **θ** EOFs), and (c) time series of θ PC1 in (top row) A_1, (second row) A_2, (third row) R_4, and (fourth row) R_5 for Feb98. In (c), circles show results of PCA, dashed lines show smoothing by a ±3 orbital average filter.

exist whose cause is not immediately clear. In channel 1, the false signal does not reveal any periodicity.

Variability is observed not only within the Feb98 and Apr98 datasets, but also from one dataset to the other. To illustrate the latter in channel 1, Fig. 9c1 shows that PC1 > 0 for all 142 orbits in Feb98 while PC1 < 0 for most orbits in Apr98 (not shown). A near-zero balance holds over the 284 orbits, and a similar balance is observed in other channels, for all three PCs. In Feb98, PC1 shows increasing trends in channels 2 and 4–5 (Fig. 9c), whereas in Apr98 (not shown) the trends are decreasing.

Relationships between the smoothed θ PC1 in different channels is shown in Fig. 10. The high correlation between the two physically similar channels 4 and 5 in Fig. 10c is expected, and its existence adds confidence to the validity of the θt analyses in this section (recall that derivation of the EOFs, and PC temporal smoothing, are done *independently* in different channels). Moreover, the reproducibility of channel 4 and 5 correlation from Feb98 to Apr98 indicates that the two VIRS window channels performed stably over the 2-month period. The correlation between channels 2 and 4 in Fig. 10b is lower compared to channels 4 and 5,
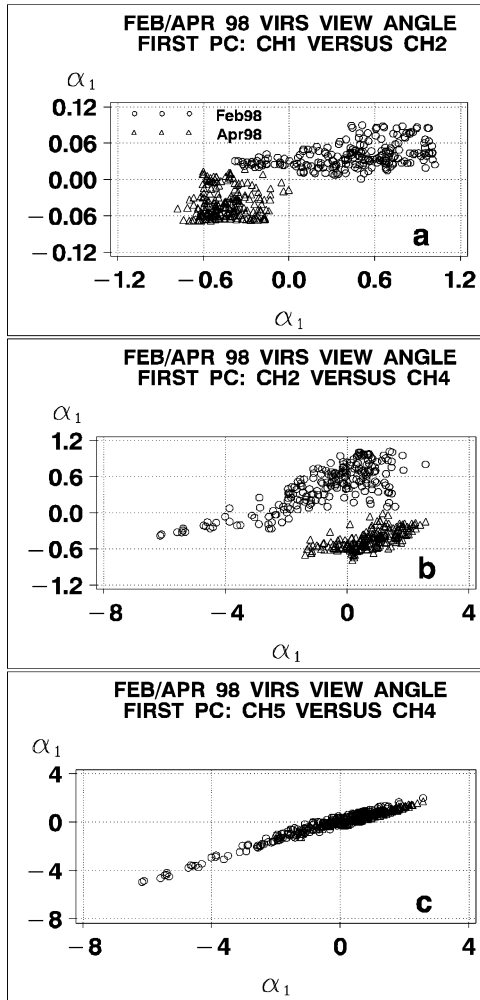
FIG. 10. Correlation between the temporally smoothed θ PC1: (top) A_1 vs A_2, (middle) A_2 vs R_4, and (bottom) R_4 vs R_5: open circle (○), Feb98; open triangle (△), Apr98.

due to the sensitivity of the thermal leak signal to the much higher atmospheric layers. The dramatic difference between the Feb98 and Apr98 clusters indicates that the thermal leak signal in VIRS channel 2 is unstable in time [cf. the Barnes–Stowe (2001, personal communication) hypothesis of the temperature of the VIRS detector as the cause]. Correlation between channels 1 and 2 in Fig. 10a is almost nonexistent within each dataset. Notable differences between Feb98 and Apr98 further suggest that accounting for temporal variations is even more important on longer timescales.

Type-3 statistics (inter- and intraorbital variability/ temporal smoothing): Type-3 rmse's in the last column of Table 1 are a factor of $\sim 3.5(\pm 0.2)$ larger compared to their type-2 counterparts in Fig. 9b in all channels, suggesting that the largest part of the pixel-to-pixel variability comes from a *suborbital* rather than *interorbital* variability. The improvement is mostly due to the ($\boldsymbol{\theta}$ average + $\boldsymbol{\theta}$ EOF1) while $\boldsymbol{\theta}$ EOF2 and $\boldsymbol{\theta}$ EOF3 do not

contribute any noticeable improvement in either channel.

Overall, the θt correction is most efficient in channel 1 where this first step of analysis is final. Figure 7b suggests that σ_{A1} is reduced ~ 2.4 times, all possible biases and trends are removed, and the θt residual cannot be improved any further. The correction is less efficient in channels 2 and 4–5, where the reductions in σ_{A2} and σ_{R4}/σ_{R5} are $\sim 20\%$ and $\sim 8\%$, respectively.

d. R_4 and time ($R_4 t$) correction

This section analyzes and removes the $R_4 t$ dependence from the θt residual in A_2. Simultaneously, the $R_4 t$ dependence is removed from the θt residual in R_5.

Type-1 statistics (interorbital variability/no temporal smoothing): Figure 11a shows three examples of the $\mathbf{R}_4$ vectors in the two VIRS channels, and Figs. 11b and 11c plot their average and STD statistics over 284 orbits. (Recall that A_2, R_4, and R_5 are now residuals of the θt correction and therefore are centered at zero.) Correlation of channel 4 with channel 5 is high (Fig. 11a2), as both window channels are sensitive to the close near-surface layers, and is much lower with channel 2 (Fig. 11a1) whose 5.2-μm thermal leak weighting function peaks significantly higher in the atmosphere. The average $\mathbf{R}_4$ vectors are close to linear in both A_2 (Fig. 11b1) and R_5, suggesting that a linear R_4 fit used in the IS00 and BS01 corrections was realistic. Approximating R_5 and A_2 with the average $\mathbf{R}_4$ vectors is much more effective in channel 5 than in channel 2. The rmse's of the respective residuals are $\sigma_{R5} \sim 0.05$ W m^{-2} sr^{-1} μm^{-1} (Fig. 11c2; $\sim 1\%$ of the range of $R_5 \sim 5$ W m^{-2} sr^{-1} μm^{-1}) and $\sigma_{A2} \sim 0.05\%$ (Fig. 11c1; $\sim 10\%$ of the range of $A_2 \sim 0.5\%$).

An important distinction from the θt analyses is that the $\mathbf{R}_4$ vectors differ in size, because the clear-sky observations may be sampled in different ranges of R_4 depending upon the dominant pattern of cloudiness over a particular orbit. The first step of the R_4 EOF analyses is thus to fill in the missing bins as they may be present during the day. This is done by substituting the $\mathbf{R}_4$ average vectors from Fig. 11b for the missing bins in each individual $\mathbf{R}_4$ vector. Note that this procedure may lead to artificial discontinuities in the individual vectors and, in turn, increase the number of EOFs needed to explain their variance. However, we found no better solution to the problem of the missing bins.

The shapes of the first three EOFs in Fig. 12a are similar in channels 2 and 5, and so are the PEVs (the first $\mathbf{R}_4$ EOF explains from 33% to 36%, the first two from 50% to 54%, and the first three from 61% to 65%). A slower convergence of the $R_4 t$ EOF process (compared to the θt) may be due to a lower signal-to-noise ratio expected due to the removal of the main part of the temporal signal by the θt correction, and due to the above-mentioned specifics of the procedure used to fill
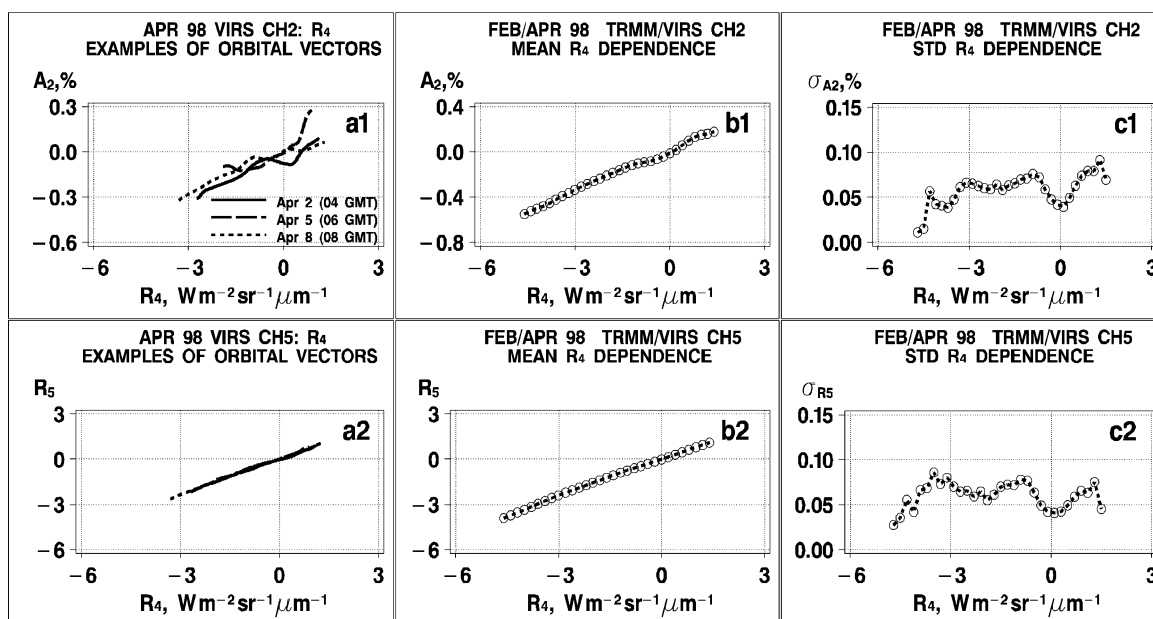
FIG. 11. Examples of (a) orbital mean $\mathbf{R}_4$ vectors, (b) average, and (c) STD $\mathbf{R}_4$ dependencies calculated over 284 orbital $\mathbf{R}_4$ vectors in (top) A_2 and (bottom) R_5.

in the missing bins, which tends to increase the noise in the individual $\mathbf{R}_4$ vectors.

Type-2 statistics (interorbital variability/temporal smoothing): The rmse of approximating the 284 $\mathbf{R}_4$ vectors with ($\mathbf{R}_4$ average + three $\mathbf{R}_4$ EOFs) and temporally smoothed PCs is shown in Fig. 12b. Contrasting this with Fig. 11c suggests that the EOF improvements in the type-2 statistics are marginal. The 7-orbit filter was

again used to separate the signal in the time series of R_4 PC1 (Fig. 12c), which appears low relative to noise (compared to the θt analyses in Fig. 9c). The correlation between the smoothed R_4 PC1 in Fig. 13 (estimated *independently* in channels 2 and 5) suggests that the temporally smoothed PC1s in A_2 and R_5 are meaningful, and adds confidence to the results of the EOF analyses.

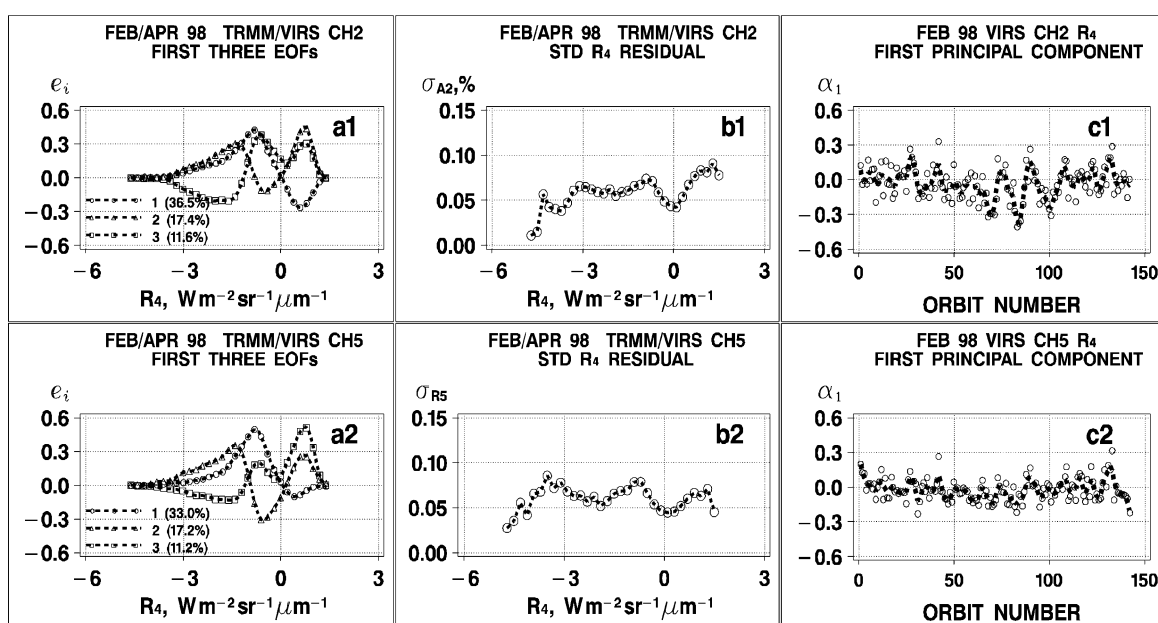*Type-3 statistics (inter- and intraorbital variability/*

FIG. 12. (a) The $\mathbf{R}_4$ EOFs with PEV superimposed, (b) residual rmsd (approximation with three $\mathbf{R}_4$ EOFs), and (c) time series of R_4 PC1 in (top) A_2 and (bottom) R_5 for Feb98. In (c), circles show results of PCA and dashed lines show smoothing by a ± 3 orbital average filter.
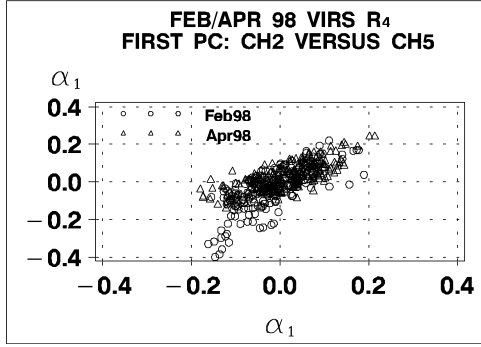
FIG. 13. Correlation between the temporally smoothed R_4 PC1: A_2 vs R_5 with open circle (○), Feb98; open triangle (△), Apr98.

temporal smoothing): Table 1 suggests that approximating residuals of the θt correction with the R_4 average reduces σ_{R5} by ~78%, and σ_{A2} by only ~20%. The R_4 EOF1 and R_4 EOF2 provide relatively small yet statistically detectable improvements in both A_2 and R_5, whereas the R_4 EOF3 is redundant. Overall, the R_4 correction reduces σ_{A2} by ~23%, a much bigger effect compared to the θt correction.

e. R_5 and time (R_5t) correction

Finally, the R_4t residual in A_2 is correlated against the R_4t residual in R_5.

Type-1 statistics (interorbital variability/no temporal smoothing): Figure 14a shows three examples of the orbital mean R_5 vectors, and Figs. 14b and 14c plot their average and STD statistics over the full ensemble of 284 orbital vectors. The average R_5 vector in Fig. 14b shows a pronounced nonlinearity, suggesting that its linear approximation in the IS00 correction was unrealistic. The missing bins in the individual vectors have been substituted for by the mean R_5 vector (Fig. 14b), similar to what was done in the R_4t analyses. The R_5 EOFs are shown in Fig. 15a, with PEVs superimposed: ~28.5% by R_5 EOF1, ~54.4% by the first two EOFs, and 62.9% by the first three.

Type-2 statistics (interorbital variability/temporal smoothing): Figure 15b shows the residual of approximating the 284 R_5 vectors with (R_5 average + three

R_5 EOFs) and temporally smoothed PCs. Time series of the R_5 PC1 for Feb98 are shown in Fig. 15c. The signal is small compared to noise.

Type-3 statistics (inter- and intraorbital variability/temporal smoothing): Table 1 suggests that approximating the residuals of the R_4t correction with the R_5 average reduces σ_{A2} by ~37%, and adding the R_5 EOFs provides only a small improvement.

f. The relative effect of the θt, R_4t, and R_5t corrections

Table 1 summarizes the relative contribution to the accuracy of correction from the different steps and elements. In channel 1, only the θt correction is needed. Approximating A_1 with (θ average + θ EOF1 + θ EOF2) effectively removes all trends in the A_1 data and reduces its rmse ~2.4 times. In channel 2, the θt correction reduces rmse by ~20%, mainly by removing the temporal (rather than angular) variability in the false signal. A much bigger contribution, however, comes from the R_4t and R_5t corrections, which reduce the rmse in A_2 ~2 times, mainly due to the removal of the average A_2 (R_4) and A_2 (R_5) dependencies. The EOF/PCA improvements are relatively minor here, due to removal of the major part of the temporal variability in the θt step. Overall, the improvement to the rmse in channel 2 from all three steps of the new correction is ~2.6 times.

5. Discussion and conclusions

False signals in the VIRS reflectance channels 1 (0.63 μm) and 2 (1.61 μm), known to exist and subject to corrections in the past, have been newly reexamined in this study. The sizeable signal in channel 2 results from the thermal leak at 5.2 μm, whereas the origin of a much smaller signal in channel 1 is unknown. Residuals of the two previous parameterizations are biased and skewed, and reveal space and thermal channels-4- and -5-specific biases. Most importantly, they also exhibit time variations with different scales whose nature is not fully understood. It is observed empirically that channel 2 time excursions are largely uncorrelated with time
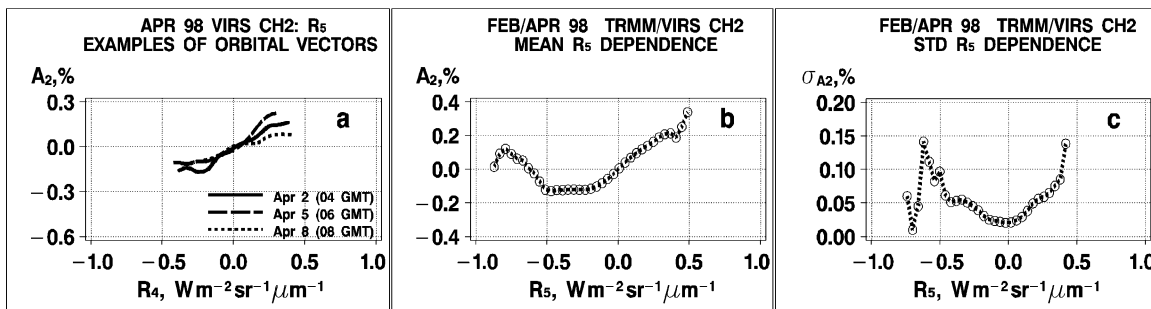

FIG. 14. Examples of (a) orbital mean R_5 vectors, (b) average, and (c) STD R_5 dependencies calculated over 284 orbits in channel 2.
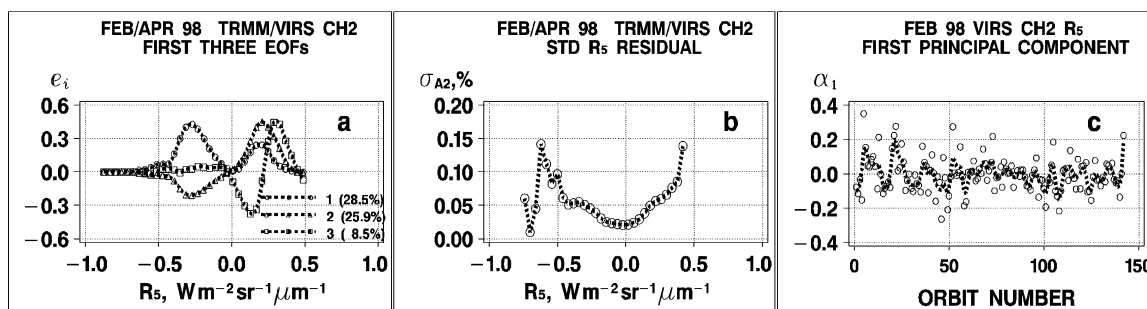
FIG. 15. (a) The $\mathbf{R}_5$ EOFs in A_2 with PEV superimposed, (b) residual rmsd (approximation with three $\mathbf{R}_5$ EOFs), and (c) time series of R_5 PC1 in A_2 for Feb98. In (c), open circles ($\bigcirc$) show results of PCA and dashed lines show smoothing by a ± 3 orbital average filter.

trends in channels 4 and 5, which in turn are highly intercorrelated between each other. This may support the Barnes–Stowe (2001, personal communication) hypothesis that attributes the temporal variability in the thermal leak signal to the instability of the temperature of the VIRS detector. It is not immediately clear if this instability affects the reflected signal in channel 2 during daytime, or measurements in any other VIRS channels.

A new empirical parameterization to the false signals was proposed and tested in this study. Its residual is centered approximately around zero (very little systematic error, or bias), distributed close to Gaussian, and its rmse is reduced. Biases with time, latitude, angles, and thermal channels 4 and 5, clearly traced in the original data, and in the residuals of the past two corrections, are lessened substantially. [Note that the proposed approach can be also tested to estimate the aerosol signal in VIRS or AVHRR channel 3 (3.8 μm) during the daytime, by subtracting the thermal component parameterized using nighttime data. The retrieved aerosol optical depth, however, is expected to be less accurate here, because the thermal signal in channel 3 is stronger compared to the thermal leak, and the aerosol signal at 3.8 μm is smaller than at 1.6 μm.]

The immediate practical objective of this study was to improve the quality of the VIRS reflectance channels, to allow a more full exploration of their aerosol signal. With the proposed correction, one is deemed to approach the limits of the VIRS aerosol information content. In channel 2, the residual of the two past corrections (using the TRMM SSF editions 1 and 2, respectively) may cause systematic errors of up to $\delta\tau_2 \sim \pm 2 \times 10^{-2}$, and random errors of $\sigma_{\tau 2} \sim 1.3 \times 10^{-2}$. The new correction effectively removes systematic biases and reduces $\sigma_{\tau 2}$ to $\sim 8 \times 10^{-3}$. Aerosol optical depth derived from the uncorrected channel 1 is biased high by $\delta\tau_1 \sim + 5 \times 10^{-3}$, on average, with an rmsd of $\sigma_{\tau 1} \sim 2 \times 10^{-3}$. The proposed correction removes the bias and reduces $\sigma_{\tau 1}$ to $\sim 1 \times 10^{-3}$.

The rmse in the Ångström exponent is approximated as $\sigma_\alpha \sim \Lambda \times \sigma_{\tau 2}/\tau_2$ (Ignatov 2002). Here, a small contribution to the α error from channel 1 was neglected, and the spectral separation factor between the channels is defined as $\Lambda = -1/\ln(\lambda_1/\lambda_2) \sim 1.07$. For typical aerosol loadings over ocean ($\tau_2 \sim 0.10$), $\sigma_\alpha \sim 0.09$. This error is about 1/3 of the typical global natural variability in the Ångström exponent [$\sigma_{\alpha o} \sim 0.30$; e.g., Ignatov and Stowe (2002)]. These estimates are preliminary, and the effect of the residual error of the correction on aerosol retrievals is yet to be explored more fully. However, it is clear that it continues to significantly impact the aerosol signal in channel 2, as well as aerosol size information under typical maritime conditions.

The above estimates of aerosol errors should be considered the "best-case scenario." The actual errors may further increase due to potential systematic differences between the daytime and nighttime clear-sky radiances caused by day/night differences in the respective cloud screening algorithms, and due to the diurnal cycle in the thermal radiances. Also, an incomplete understanding of the physical mechanisms behind the derived EOFs and PCs, and the unknown origin of the false signal in channel 1, may further increase errors during application of the nighttime parameterizations to daytime data.

These analyses further illustrate the point made elsewhere (Ignatov 2002; Ignatov and Stowe 2002) that retrieval of aerosol properties from satellite is a complex data analysis problem, not fully reduced to the theoretical aspect of the retrieval algorithm, such as an adequate characterization of the aerosol microphysics, or radiative transfer modeling. The data quality may seriously limit the degree of sophistication of the aerosol algorithm, and affect its information content and accuracy. In a low-radiance regime used for aerosol retrievals, radiometric uncertainties significantly contribute to the aerosol retrieval errors.

Current results may also serve as a feedback from the aerosol remote sensing community to the instrument/calibration community, by quantitatively emphasizing the importance of accurate radiometric characterization of satellite instruments, and alerting them to the severe and time consuming effort of correction, with an uncertain result. It is recommended that technical problems similar to those discussed here be avoided in the future for aerosol remote sensing oriented sensors.

REFERENCES

Barnes, R. A., W. L. Barnes, C.-H. Lyu, and J. M. Gales, 2000: An overview of the VIRS radiometric calibration algorithm. *J. Atmos. Oceanic Technol.,* **17,** 395–405.

Geier, E. B., R. N. Green, D. P. Kratz, P. Minnis, W. Miller, S. K. Nolan, and C. B. Franklin, 2001: Clouds and the Earth's Radiant Energy System (CERES) data management system: Single Scanner Footprint TOA/surface fluxes and clouds (SSF) collection document. Release 1, version 6, 194 pp; and appendixes. [Available online at http://asd-www.larc.nasa.gov/ceres/collect_guide/CG_SSF.pdf.]

Ignatov, A., 2002: Sensitivity and information content of aerosol retrievals from AVHRR: Radiometric factors. *Appl. Opt.,* **59,** 335–362.

——, and L. Stowe, 2000: Physical basis, premises, and self-consistency checks of aerosol retrievals from TRMM VIRS. *J. Appl. Meteor.,* **39,** 2259–2277.

——, and ——, 2002: Aerosol retrievals from individual AVHRR channels. Part II: Quality control, probability distribution functions, information content, and consistency checks of retrievals. *J. Atmos. Sci.,* **59,** 335–362.

Kato, S., N. Loeb, and K. Rutlege, 2002: Estimate of top-of-atmosphere albedo for a molecular atmosphere over ocean using Clouds and the Earth's Radiant Energy System (CERES) measurements. *J. Geophys. Res.,* **107,** 4396, doi:10.1029/2001JD001309.

Kummerow, C., W. Barnes, T. Kozu, J. Shiue, and J. Simpson, 1998: The Tropical Rainfall Measuring Mission (TRMM) sensor package. *J. Atmos. Oceanic Technol.,* **15,** 809–817.

——, and Coauthors, 2000: The status of the Tropical Rainfall Measuring Mission (TRMM) after two years in orbit. *J. Appl. Meteor.,* **39,** 1965–1982.

Lanczos, C., 1988: *Applied Analysis.* Dover, 539 pp.

Loeb, N., and S. Kato, 2002: Top-of-atmosphere direct radiative effect of aerosols over the tropical oceans from the Clouds and the Earth's Radiant Energy System (CERES) satellite instrument. *J. Climate,* **15,** 1474–1484.

Minnis, P., L. Nguyen, D. Doelling, D. Young, W. Miller, and D. Kratz, 2002: Rapid calibration of operational and research meteorological satellite imagers. Part I: Evaluation of research satellite visible channels as a reference. *J. Atmos. Oceanic Technol.,* **19,** 1233–1249.

Rutan, D., and T. Charlock, 2002: Atmospheric net fluxes inferred from CERES/SARB fluxes. Preprints, *11th Conf. on Atmospheric Radiation,* Ogden, UT, Amer. Meteor. Soc., 156–159.

Trepte, Q., Y. Chen, S. Sun-Mack, P. Minnis, D. Young, B. Baum, and P. Heck, 1999: Scene identification for the CERES cloud analysis subsystem. Preprints, *10th Conf. on Atmospheric Radiation,* Madison, WI, Amer. Meteor. Soc., 169–172.

Wielicki, B. A., B. R. Barkstrom, E. F. Harrison, R. B. Lee III, G. L. Smith, and J. E. Cooper, 1996: Clouds and the Earth's Radiant Energy System (CERES): An earth observing system experiment. *Bull. Amer. Meteor. Soc.,* **77,** 853–868.